4.2 Newly Constructed Beamlines

4-2-1 BL-1A

BL-1A was constructed as a joint project based on two separate proposals: "Study on correlated electron systems by a new research network" and "Crystal structure analysis of strongly correlated electron systems". The former proposal is being conducted by five institutes: the Institute of Materials Structure Science (IMSS), the Institute for Materials Research (IMR), the Institute for Solid State Physics (ISSP), the Institute for Molecular Science (IMS), and the Institute for Chemical Research (ICR) at Kyoto University. The latter proposal is being conducted by the Correlated Electron Research Center. The aim of the former proposal is to make a new research field at the boundary of material physics and material chemistry by creating a new "collaboratory" research network.

What is the "Collaboratory system"?

The word "Collaboratory" was coined by joining the two words "collaboration" and "laboratory", and describes a new joint research style using computer and network technology. In order to expand the material science fields, a special new beamline equipped with facilities to enable video net-meeting and in some cases remote operation was planned. The new equipment will enable large research teams belonging to several different institutes to conduct experiments together at the new beamline. Even though only a few members of the team can be present at the beamline, they will be able to communicate in real time with their home base team and teams at other institutes using the video net-meeting system.

Items for control

A multipurpose diffractometer (Fig.1) at BL-1A can be operated by researchers at external sites using application-sharing under the collaboratory system. As shown in Fig. 2, this system consists of several personal computers for control and data analysis, on which the

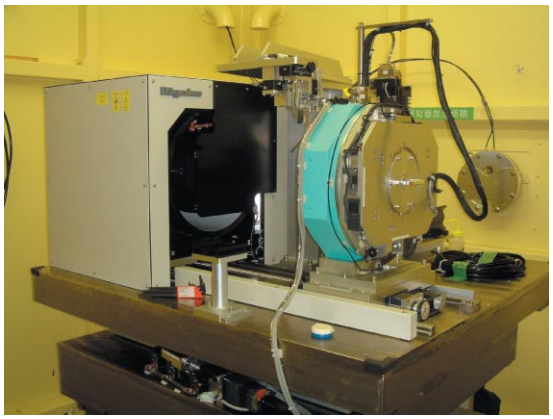

Figure 1
Multi purpose X-ray diffractometer.

Figure 2
Personal computers for control system.

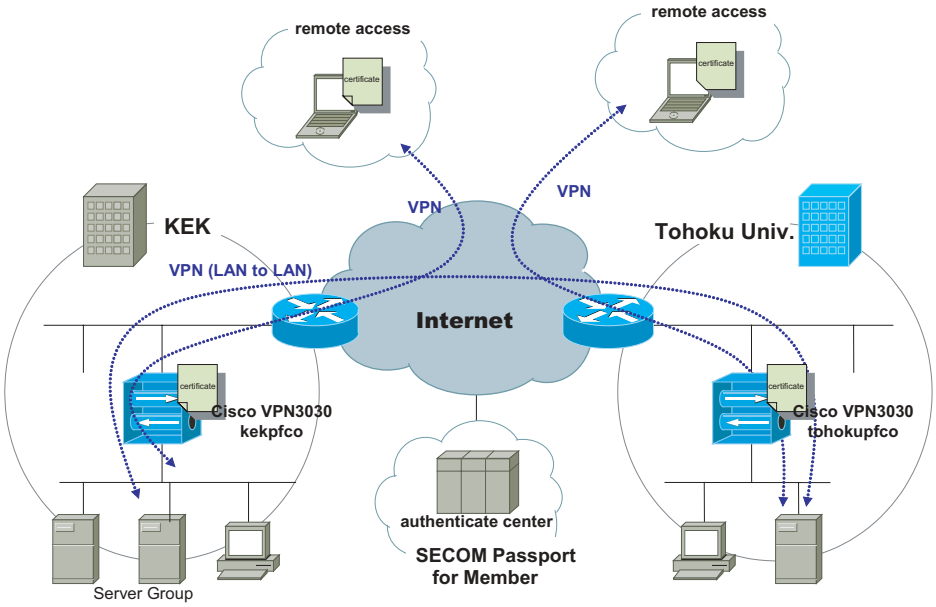

Figure 3
Network for the "Collaboratory" system.

application sharing system also runs.

Network

An exclusive and secure network is required for the collaboratory system. The collaboratory network has 2 VPN (Virtual Private Network) routers. The operating researchers can connect to this network through the VPN router. Figure 3 shows the composition of the network.

The Collaboratory system is being conducted by five institutes; IMS, IMR, ICR, ISSP, and IMSS, as mentioned above. The beamline is used by researchers from other institutes belonging to this project (Fig. 4.).

High level video net-meeting has become possible with the very high bandwidth data transmission (up to 10 Gbps) available on the SuperSINET network which connects principal universities and institutes throughout Japan. In order to ensure a secure network environment, we also use a VPN system. Using Multi Connected Unit servers connected among multi points, it is possible to access the network at the same time and discuss with researchers who are in different institutes.

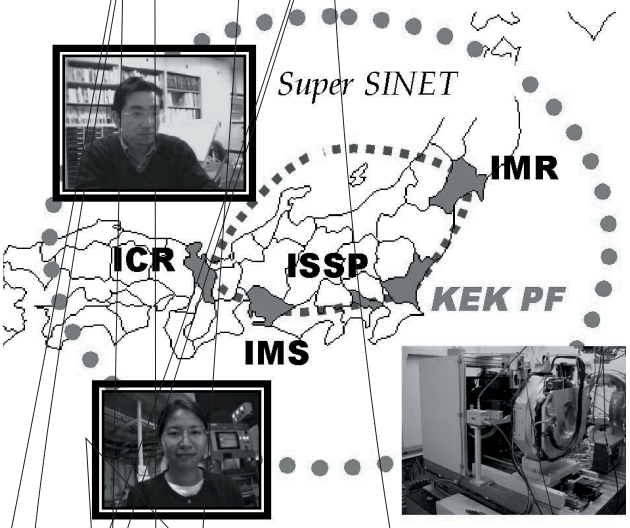

Figure 4
Image of Multi-point video net-meeting and remote operation.

4-2-2 BL-5A

Outline

BL-5A is a new beamline at the PF 2.5 GeV ring designed for high-throughput protein crystallographic experiments. The design of the beamline is optimized for efficient multiwavelength anomalous divergence (MAD) experiments, and is similar to that of AR-NW12A which was constructed during FY2002. The precision of the sample axis positioning and the size of the active area of the X-ray CCD detector are superior to those of AR-NW12A, so BL-5A is particularly suited to data collection using micro-crystals with large cell dimensions at high resolution. The new beamline was constructed during FY2003. After observation of the first beam on 29th September 2003, commissioning of the beamline components and test experiments by external users were carried out. BL-5A has been open for public use since April 2004.

Light source and optics

Figure 5 shows top and side views of the design of the beamline, and the locations and specifications of the main optical components are summarized in Table 1. Compared to AR-NW12A, the main differences are (1) the light source is a multi-pole wiggler (MPW), and (2) a direct micro-channel water cooling system is used for the monochromator crystals. The beam from the MPW is trimmed by the front-end slits to limit the divergence to 0.5 mrad (H) × 0.24 mrad (V), and passed through the collimating mirror, the double crystal monochromator and a focusing mirror before delivered to the sample position. The focal point is 250 mm downstream from the sample position, with a focusing ratio of about 2:1.

The characteristics of the beam at the sample position are summarized in Table 2. The energy resolution of the beam was estimated from the full width at half maximum (FWHM) of the rocking curve using Si(111), and the beam size was measured by silt scanning. The beam intensity was estimated using a PIN photo-diode at the sample position, with 0.2 × 0.2 mm slits and a 0.2 mm ϕ pin-hole.

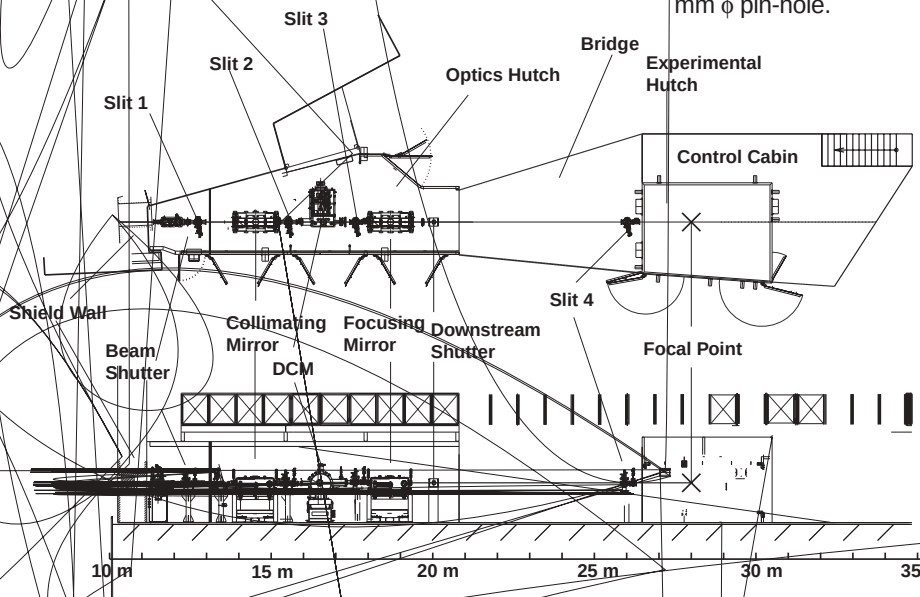

Figure 5
Top (upper panel) and side (lower panel) views of the design of beamline BL-5. The storage ring is located on the left hand side.

Table 1 Specification of the optical components of BL-5A.

Insertion device	Type: multipole wiggler Length of period: 120 mm Number of periods: 21 Magnetic field: max 1.4 Tesla
Collimating mirror (14.5 m from the source)	Type: flat-bent Material: Rh-coated Si single crystal Size (mm): 1000(L) × 80(W) × 70(T) Glancing angle: 3.5 mrad Radius of curvature: 8286 m
Double crystal monochromator (16.5 m)	Material: Si(111) Fixed exit: numerical link Cooling system: direct water cooling with micro-channel Energy range: 6.5 – 17 keV
Focusing mirror (18.7 m)	Type: bent-cylindrical Material: Rh-coated Si single crystal Size (mm): 1000(L) × 100(W) × 60(T) Glancing angle: 3.5 mrad Radius of curvature: 43.55 mm, 5333 m

Table 2 Characteristics of the beam.

	Measured	Simulated
Energy resolution $\Delta E/E$ at 12.7 keV	2.5×10^{-4}	2.0×10^{-4}
Beam size at the focal point (mm) at 12.7 keV	1.5 (H) 0.3 (V)	0.4 (H) 0.3 (V)
Beam intensity (photons/sec) (0.2 × 0.2 mm slit + 0.2 mm ϕ pin-hole)	1.0×10^{11}	6.0×10^{11}

Experimental station

The basic design of the experimental station is almost the same as that of AR-NW12A, with higher precision positioning of the sample axis and a CCD detector with a larger active area, making the beamline suitable for experiments with crystals of complex proteins, which are often very small in size with large cell dimensions. The large active area of the detector also allows data collection with low energy X-ray at high resolution, which was difficult using the previous CCD detectors. Figure 6 shows the precision of the sample axis positioning, which has a sphere of confusion of less than 1 µm.

The CCD-type X-ray detector (ADSC Quantum 315, see Fig. 7) has an active area of 315 mm^2 and a pixel size of 51 µm. One image frame (6144 × 6144 × 2 byte in full resolution mode) can be read out in about one second, and the total dead time including read-out is around 2.0 seconds per frame. The exposure time for one frame is typically around 5 seconds. In total, the time necessary to collect one data set (1 degree oscillation and 180 frames) is around 20 minutes, giving a data acquisition speed similar to the fastest beamlines in the world. In the future, this will enable fine phi-slicing experiments requiring thousands of frames per data set.

For error-free and high throughput operation of the beamline, various components such as the attenuator, two four-blade slits, the X-ray shutter and other equip-

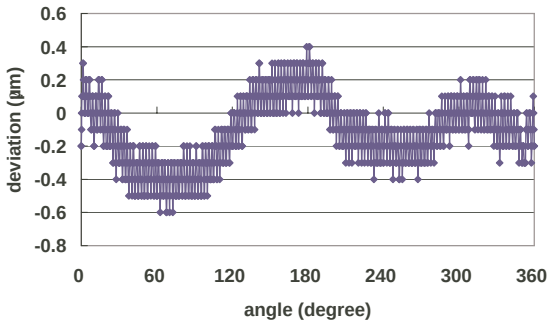

Figure 6
Deviation of the sample axis.

Figure 7
CCD detector (Quantum 315) on the experimental base.

ment near the sample (for example the beam stop) are all motorized to allow automatic data collection using the sample exchange robot and the control software developed for the protein crystallography beamlines.

Computing environment for high-throughput data analysis

We have installed six Linux PCs for data processing and phase calculations at the beamline. The diffraction images are stored on a RAID file server with 2-TB storage. Three PCs are prepared for data backup with IEEE1394 and USB2.0 interfaces. These computers are all connected by gigabit Ethernet for rapid data transfer. In addition to the local resources, a central server for all the protein crystallography beamlines is available for data storage and processing.

Scientific activities

—Reclassification of Inverting Phosphorylases Based on Structure Determination—

Enzymes involved in the formation or cleavage of glycosyl linkages are mainly categorized as belonging to either the Glycoside Hydrolase (GH) or Glycosyl Transferase (GT) classes (see the CAZy website at http://afmb.cnrs-mrs.fr/CAZY/). Each class comprises of dozens of families classified on the basis of amino acid sequence similarity. Phosphorylases catalyze the cleavage of glycosidic bonds by adding inorganic phosphate to generate glycosyl-phosphates (phosphorolysis). Since the energy of the glycosyl-phosphate bond is not as high as that of a glycosyl-nucleotide, the reactions are reversible. Therefore, phosphorylases can be employed for both the synthesis and degradation of sugar chains. Phosphorylases have been assigned EC numbers of glycosyltransferases (2.4.1.-) according to the apparent reaction scheme. However, they occupy a peculiar position in the CAZy database as they are classified across the GH and GT classes.

Vibrio proteolyticus chitobiose phosphorylase (ChBP) previously belonged to the GT-36 family. It catalyzes the phosphorolysis of GlcNAc-b-1,4-GlcNAc (chitobiose) into a-GlcNAc-1-phosphate and GlcNAc with inversion of the anomeric configuration (inverting phosphorolysis). As the rst structure of a GT-36 enzyme, we determined the crystal structure of ChBP using beamlines BL-6A and NW12A [1]. ChBP comprises of b sandwich and (a/a)6 barrel domains, constituting a distinct structure from GT folds (Fig. 8). Instead, it shows signicant structural similarity with the inverting glycoside hydrolases (GH-15 glucoamylase and GH-65 maltose phosphorylase). Moreover, the ternary complex of ChBP with GlcNAc and SO4 was the rst structure of an inverting phosphorylase in a complex with both sugar and anion, and revealed a pseudo-ternary complex structure of enzyme-sugar-phosphate (Fig. 9). Considering the topology of the active site structure, we concluded that the enzymatic phosphorolysis begins with the direct nucleophilic attack by phosphate of the glycosidic bond with the aid of a conserved general acid residue (Asp492) which donates a proton to the glycosidic oxygen atom and then proceeds through an oxocarbenium cation-like transition state. The proposed reaction mechanism for the inverting phosphorylase is similar to that for inverting glycoside hydrolases, except that the molecule attacking the C1 atom of the glycoside is water activated by a general base residue in the inverting GH reaction. The similarities of the overall structures and catalytic mechanisms between the ChBP and GH enzymes led to a signicant reorganization of the CAZy database; the GT-36 family was deleted and reclassified into a novel GH family, GH-94. This type of reclassi fication, in which a family travels across two functionally distinct classes, is unprecedented. This structural and functional similarity of inverting glycoside hydrolases and inverting phosphorylases suggests a possible evolutionary relationship.

We have also succeeded in obtaining crystals of cellobiose phosphorylase (CBP) and collected diffraction data up to 2.1 Å resolution at BL-5A [2]. Among the GH-94 enzymes, CBP is the enzyme most used for studies on substrate specificity and reaction mechanisms, and its application for practical oligosaccharide

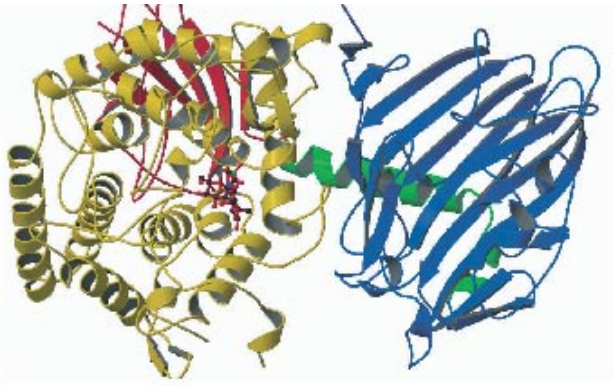

Figure 8
Overall structure of ChBP (N-terminal domain, blue; linker helices,green; α-helical barrel domain, yellow; C-terminal domain, red). The bound GlcNAc molecules are shown as a ball-and-stick model.

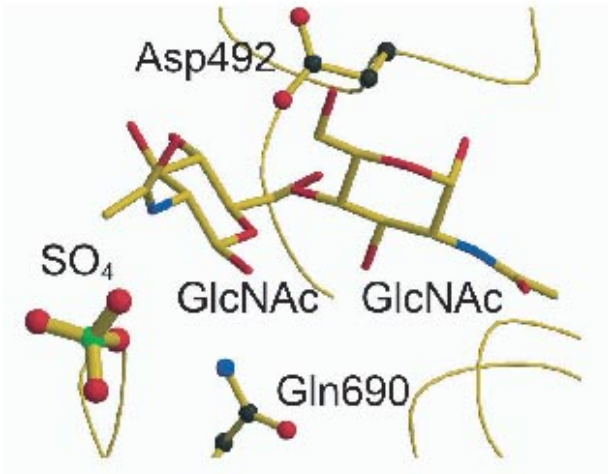

Figure 9
Active site of ChBP.

synthesis has been established. The 3D structure of CBP will help technical developments in the production of new functional oligosacchalides.

References

[1] M. Hidaka, Y. Honda, M. Kitaoka, S. Nirasawa, K. Hayashi, T. Wakagi, H. Shoun and S. Fushinobu, *Structure*, **12** (2004) 937.

[2] M. Hidaka, M. Kitaoka, K. Hayashi, T. Wakagi, H. Shoun and S. Fushinobu, *Acta Cryst. D.*, **60** (2004) 1877.

4-2-3 BL-17A

Four new short straight sections were created as part of the "Straight-Section Upgrade Project" of the PF 2.5 GeV ring during a six-month shutdown in the first half of FY2005 [3]. The new short-gap undulator SGU#17 was newly designed for one of the short straight sections. The high brilliance beam derived from SGU#17 offers unique possibilities for protein crystallographic experiments at the Photon Factory: microcrystal structure analysis and structure determination using the softer X-rays. The extremely small beam size of the short-gap undulator source together with advances in X-ray optics allows outstanding performance to be obtained at modest cost even at a 2nd generation synchrotron facility.

Along with the construction of the new BL-17A, the beamline previously used for protein crystallography at BL-18B was closed and the activities of the old BL-17A, B and C were transferred to a reconstructed BL-18B. This scrap-and-build of BL-17 and BL-18B began at the end of February, 2005 and was successfully completed in September 2005.

The schematic layout of BL-17A is shown in Fig.10. The undulator has a periodic length of 16 mm and effectively 29 periods. The minimum gap is 4.5 mm, giving a K_{max} of 1.27. The corresponding tuning ranges of the 3rd and the 5th harmonics are 6-9 keV and 11-13 keV. A water-cooled four-blade slit immediately downstream of the shield wall limits the horizontal beam divergence to 0.1 mrad. After the slit there is a branch beam shutter and a set of wire monitors for beam profile measurements. A vertically-deflecting double-crystal monochromator (DCM) is located 17.5 m from the light source. It covers a wide energy range from 6 to 13 keV with a fixed beam exit using a numerical link mechanism [4]. The crystals are cooled by an indirect liquid-nitrogen circulation system to reduce crystal deformation caused by high heat load. Following the DCM, a K-B mirror system is used for fine focusing. Two sets of flat mirror benders are located at 24.0 m for vertical focusing with a focusing ratio of 2:1, and at 30.8 m for horizontal focusing with a ratio of 6:1. To keep the surfaces of the mirrors

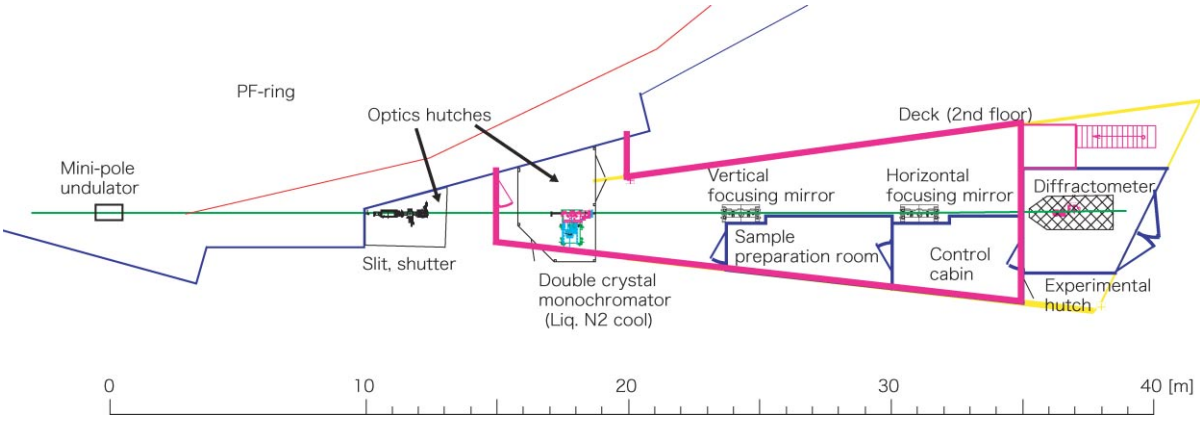

Figure 10
Schematic layout of the BL-17A.

clean, the mirror chambers are separated from the DCM by a 0.2 mm thick beryllium window, and all sections of the beam line are kept at high vacuum by oil-free pumps. Both mirrors are Rh-coated Si crystals which show good performance; roughness of 1.7 Å rms and 2.0 Å rms, and tangential slope errors of 0.75 μ-rad rms and 0.95 μ-rad rms. The cut-off energy is approximately 15 keV with a glancing angle of 4.0 mrad for diffraction studies using soft X-rays (i.e. 6 keV). The second mirror has an elliptically-bent surface which is achieved by the "Arm Method" mirror bender, to reduce the aberration of the highly asymmetric 6:1(H) focusing ratio [5]. Consequently, the beam size at the focal point (36 m) is estimated to be around 10 times smaller than those of the two high-throughput beam lines, AR-NW12A and BL-5A of the Photon Factory. The beam intensity at the focal point using collimator size of 20 μm × 20 μm is calculated to be higher than 10^{10} photons/sec at 12.4 keV and 10^{11} photons/sec at 6.5 keV.

The beam line has three hutches, two optics hutches and an experimental hutch. There are two additional rooms for users: a control cabin and a sample preparation room. The control cabin provides users with an experimental environment similar to those of their home laboratories, allowing them to concentrate on their experiments without disturbance. Above the hutches and the rooms there is a large deck for computational work such as data processing, analysis and archiving. A combination of a high-speed network and a unified user interface makes it possible to access diffraction data in the same way as at the beam line even after the end of beamtime.

After the completion of the construction work the first beam was delivered at BL-17A on October 7 2005, with commissioning progressing after the first beam. The preliminary performance is as follows. The focused beam size (FWHM) using the K-B mirror system is about 32.9 μm (V) × 233.5 μm (H). The photon flux at 12.4 keV with collimation slit widths of 100 μm × 100 μm, 40 μm ×40 μm and 20 μm × 20 μm are 7.72 × 10^{10} photons/sec, 2.22 × 10^{10} photons/sec and 6.56 × 10^{9} photons/sec respectively. This preliminary result is about 60 % of the expected performance, and it is expected that improvements can be made by optimizing the undulator source and beamline optics.

A single-axis diffractometer is being designed with the final goal of 100 to 200 nm rotation error for micron-size crystals and will be installed at the end of January 2006. Test experiments will begin at the end of February 2006 and general user operation will commence in the spring of 2006.

References

[3] S. Asaoka, K. Haga, K. Harada, T. Honda, Y. Hori, M. Izawa, T. Kasuga, M. Kobayashi, Y. Kobayashi, H. Maezawa, Y. Minagawa, A. Mishina, T. Mitsuhashi, T. Miyajima, H. Miyauchi, S. Nagahashi, T. Nogami, T. Obina, C. O. Pak, S. Sakanaka, Y. Sato, T. Shioya, M. Tadano, T. Takahashi, Y. Tanimoto, K. Tsuchiya, T. Uchiyama, A. Ueda, K. Umemori, and S. Yamamoto, *AIP Conf. Proc.*, **705** (2004) 161.

[4] H. Kawata, T. Mori, H. Adachi, N. Matsugaki, A. Koyama and M. Nomura, *AIP Conf. Proc*., **705** (2004) 663.

[5] N. Kamachi, K. Endo, H. Ohashi and T. Ishikawa, *MEDSI2002 Proc.*, (2002) 113.

4-2-4 Construction of a New Undulator Beamline BL-28A for High-resolution ARPES

BL-28 is a helical undulator beamline which covers the photon energy range of 30 to 300 eV (Table 3), and is suitable for the electronic structure study of nanomaterials, strongly correlated materials, and surfaces. We have restructured the beamline and constructed a new endstation for high-resolution angle-resolved photoemission (ARPES) experiments. A high-resolution ARPES beamline has been strongly demanded by many users for a long time. The main purpose of this beamline is ARPES studies on high transition temperature (high-Tc) superconductors and nanomaterials fabricated by in situ combinatorial pulsed-laser deposition (PLD) systems. To perform high-resolution ARPES experiments for high-Tc superconductors and nanomaterials, high energy-resolution as well as high photon flux is needed. We have chosen a variable-included–angle, varied-line-spacing plane grating monochromator which satisfies the requirements for both high energy resolution and high photon flux.

The monochromator consists of three mirrors (M0, M1, M2) and one grating. M0, M1, and the grating experience considerable heat load from the undulator and are cooled by an indirect water-cooling system. The monochromator has no entrance slit, allowing for higher photon flux and high energy-resolution to be achieved over a wide energy range. The monochromator is designed to cover the photon energy range of 30 to 1,000 eV and will be used unmodified after the future renewal of the undulator. Precise control of the mirrors and gratings can be achieved by in-vacuum rotary encoders with an on-line vibration diagnostic system.

The commissioning of BL-28A was carried out during the summer shutdown period of 2004. A photograph of the newly-built BL-28A is shown in Fig. 11. From the end of beamtime in 2004, adjustments of the new beamline and setup of the ARPES endstation were carried out. Evaluation of the energy resolution of the beamline was carried out with rare-gas photoionization measurements. Figure 12 shows the photoionization yield of Ar 3*s* to n*p* photoexcitation spectra recorded around 30 eV. Distinct peaks up to n=30 were clearly observed with widths of less than 1 meV, indicating an energy resolving power (E/ΔE) of more than 30,000. The photon flux was measured with a calibrated photo-

Table 3 Specifications of the new undulator beamline BL-28.

Photon energy	30 ~ 300 eV
Energy resolution (E/ΔE)	5,000 ~ 10,000
Photon flux	> 10^{12} photons/sec at the highest energy resolution
Spot size	350 μm (H) x 50 μm (V)

Figure 11
Photograph of the newly-built beamline BL-28A.

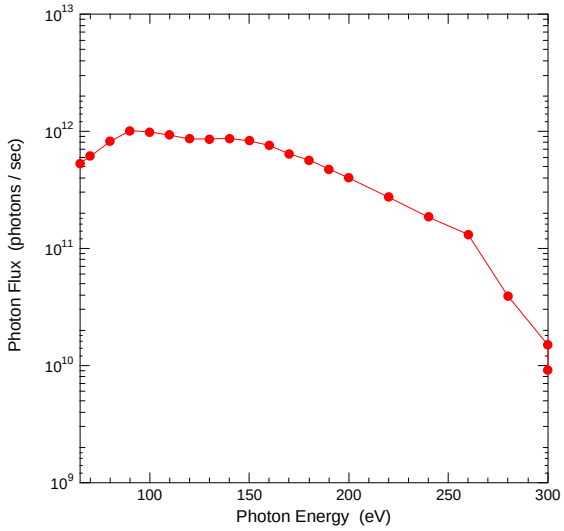

Figure 13
Observed photon flux with the monochromator set to maximum energy resolution.

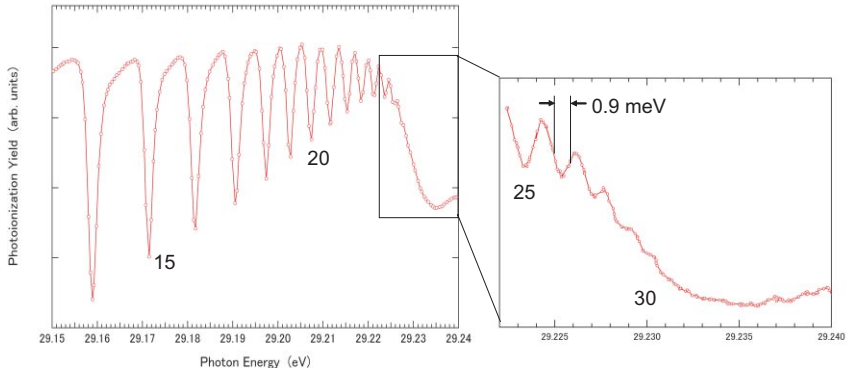

Figure 12
Photoionization yeild of Ar 3s to np around 30 eV.

diode. Figure 13 shows the observed photon flux with the monochromator set to the maximum energy resolution. These results indicate that the beamline exhibits both high energy-resolution and high photon flux.

For the high-resolution ARPES endstation, we have selected a Gammadata Scienta SES-2002 analyzer. We have also developed a new manipulator with a multi-axis goniometer to perform automated Fermi surface mapping and high-throughput ARPES experiments. Construction of the ARPES endstation system was done in collaboration with three user groups. Figure 14 shows a photograph of the ARPES endstation at BL-28A. The new ARPES beamline will be open for users in FY2006 and the branch BL-28B will be constructed in summer shutdown of 2006.

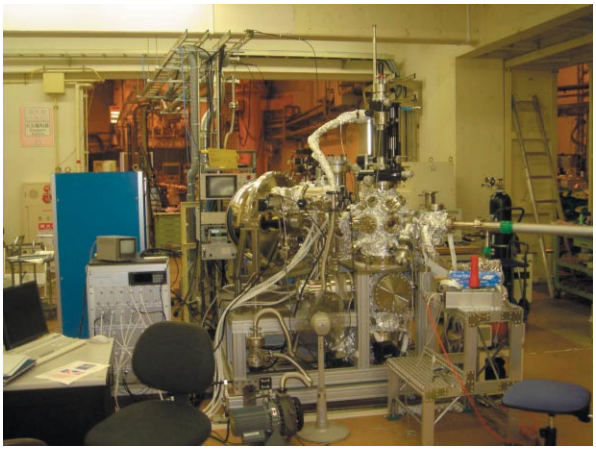

Figure 14
Photograph of the ARPES endstation at BL-28A.

4-2-5 AR-NW2A

The reconstruction and reinforcement of the PF-AR were approved in the supplemental budget of 1999. It then became possible to start the renewal of the accelerator (vacuum system, monitor system and magnet system etc.) and construction of an X-ray undulator beamline (AR-NW2A) for protein crystallography as well as time-resolved XAFS experiments. Before 1999, a small experimental area had been constructed for the AR-NW2A in the space initially designed as an electron-positron colliding area.

In 2000, a second supplemental budget was approved for the construction of a new experimental hall in the northwest part of the PF-AR, as well as one more X-ray undulator beamline (AR-NW12A). We thus decided that beamline AR-NW2A would be constructed as a dedicated beamline for XAFS experiments and that AR-NW12A would be dedicated to protein crystallography based on the multiple-wave-length anomalous diffraction (MAD) method.

The specifications of the new AR-NW2A beamline are as follows:

(1) In order to conduct conventional XAFS experiments, it is essential to realize a good energy tunability in the 5 ~ 25 keV energy range.

(2) The photon flux of monochromatized X-rays at the sample position should be at least 10^{13} photons/s for a beam size less than 0.5 × 0.5 mm^2.

(3) For time-resolved experiments with an energy-dispersive XAFS arrangement, it is necessary to focus white X-rays in the vertical direction, with a relatively wide energy spread of the undulator radiation.

Figure 15 shows the plan view of the beamline. In order to achieve the above specifications, the beamline was designed as follows. The insertion device is an in-vacuum undulator with a period of 40 mm and the number of periods is 90, covering an energy range of 5~25 keV by using the 1st, 3rd and 5th harmonics of the undulator radiation. The device has optional mechanics to make a tapered undulator in order to obtain a wider energy spread ($\Delta E/E$ ~ 10^{-1}) for the 3rd harmonics. The front end consists of a fixed mask, a beam-position mon-

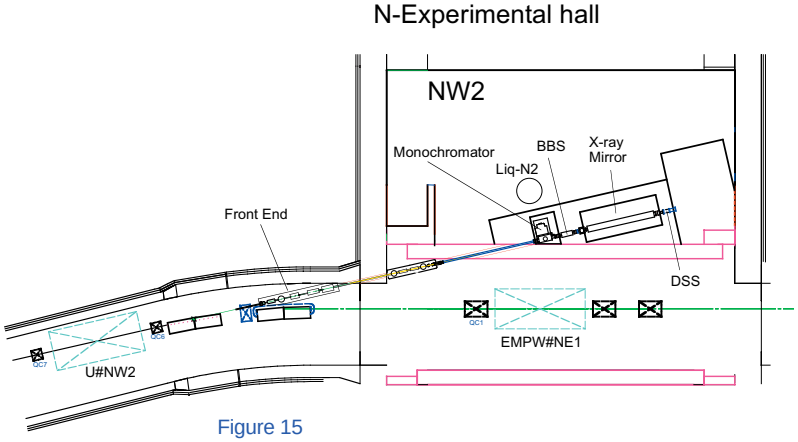

Figure 15
Schematic layout of the new beamline AR-NW2.

Figure 16
Photographs of the AR-NW2A. (Right) The double-crystal monochromator and mirrors have been installed in a hutch on the shield wall of the ring. The multi-pole wiggler for the beamline AR-NE1 (EMPW#NE1) is seen just inside the wall. (Left) Cryogenic cooling system for the monochromator crystal is set outside the hutch.

itor, an absorber, a beam shutter, graphite heat absorbers, XY-slits for white X-rays and Be windows. The main optical components are a double-crystal monochromator and a focusing mirror system, which are located 22.5 m and 25 ~ 28 m from the center of the insertion device, respectively (Fig. 16). The double-crystal monochromator consists of flat Si(111) crystals which are cooled with liquid nitrogen in order to reduce any deformation caused by heat load. The circulation of liquid nitrogen is realized by a closed-loop system with two GM-refrigerators with cooling powers of 170 W each. Thus it is possible to handle incoming heat powers of up to about 300 W. The focusing mirror system has 4 mirror assemblies: a bent cylindrical mirror for double focusing of X-rays, a bent flat mirror for vertical focusing, and a double-mirror system (cut-off mirrors) to reduce the intensity of higher harmonics. When a doubly focused beam is necessary for high-flux XAFS experiments a bent cylindrical mirror and a double-mirror system will be used. The double-focusing mirror is replaced by a flat mirror for time-resolved experiments in the energy-dispersive XAFS geometry. Then, one of the cut-off mirrors will be bent at the meridian direction to allow vertical focusing of the white X-rays.

The first beam from the undulator was observed on February 4 2002, after which the commissioning of the monochromator and mirror system progressed. One of the characteristic points of the monochromator is the usage of a relatively long second silicon crystal (~200 mm) along the beam direction. Using a long crystal makes it possible to avoid using a mechanical translation stage for the second crystal, which is needed to realize a fixed exit position for the monochromatized X-rays. Figure 17 shows the rocking curves of Si (111)(11.39 keV) and (333)(34.17 keV) diffractions at the minimum gap of the undulator (10 mm), corresponding to K=3. As shown in this figure, the width of the (333) diffraction was less than 1 arcsec, and we could not observe any heat load problem. After optimizing several parameters, it is possible to keep the deviation of the beam position at the experimental hutch less than 0.1 mm in both horizontal

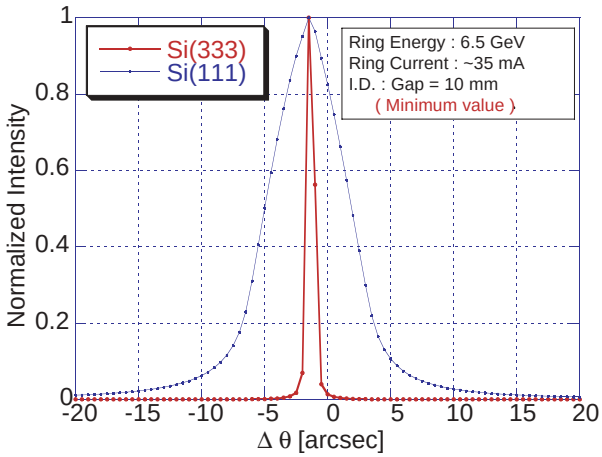

Figure 17
Rocking curves of Si(111)(11.39 keV) and (333)(34.17 keV) diffractions of the double crystal monochromator at the condition of the minimum gap of the undulator 10 mm, which corresponds to K=3. The total radiation power on the monochromator crystal was 300 W. There is no observable heat load problem on the perfomance of the monochromator.

and vertical directions when scanning the monochromator from 5 to 25 keV.

Several spectra of the undulator radiation at different K-values have been observed. Figure 18 shows the taper dependence of the spectrum of the 3rd harmonics of the undulator radiation, which has a K-value of 1.5. The energy spread of the 3rd harmonic is about 300 eV for a normal undulator (taper=0.0 mm). On introducing the tapered mode, the shape of the peak becomes flatter and wider. When the tapered angle is set to ~1.0 mm/3600 mm (Taper =1.0 mm in Fig. 18), the energy spread becomes 1 keV, which is a wide enough energy region for energy-dispersive XAFS experiments.

The focusing mirror system has 4 mirror assemblies, as described above. Figure 19 shows focused beam profiles along the vertical and horizontal directions obtained from ray-tracing calculations. The observed values of 0.15 mm and 0.45 mm in the vertical and horizontal directions are reasonable, as also shown in Fig. 19. The preliminary test of the vertical focusing with a bent flat mirror was made and a 0.07 mm focused beam

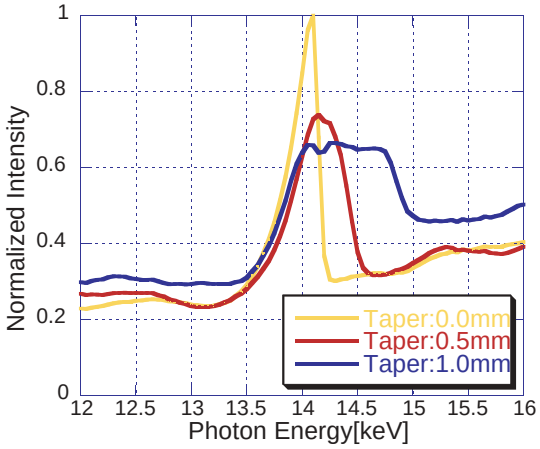

Figure 18
Tapered mode dependence of the spectrum on 3rd hamonics undulator sychrotron radiation, whose K-value is equal to 1.5. The energy spread of the 3rd hamonics is about 300 eV for the case of the normal undulator (taper=0.0 mm). On introducing the tapered mode, the shape of the peak becomes flat and the spread becomes wider.

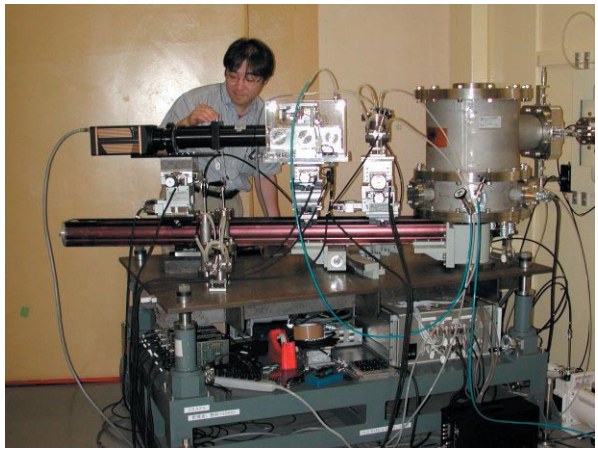

Figure 20
DXAFS apparatus with Dr. Y. Inada.

was obtained at the experimental hutch.

The photon flux was measured at a monochromatic energy of 12.4 keV using the 3rd harmonic of the undulator synchrotron radiation. Performance is consistent with calculations, and the total flux through an area of 0.4 × 0.5 mm^2 is about 5 × 10^{12} photons/s with a stored current of 50 mA. Some test XAFS measurements have been performed in both the step-scanning and energy-dispersive modes. Here we introduce an energy-dispersive XAFS (DXAFS) study on a catalytic reaction process as an example. A Cu catalyst supported on zeolite (Cu/ZSM-5) for NOX reduction was prepared and set in the apparatus (shown in Fig. 20). Time-resolved DXAFS spectra were measured during the catalytic reaction process which was initiated by the sudden introduction of a mixed gas of CO (6.9 kPa) and NO (26.6 kPa) at 500°C. Figure 21(a) shows the DXAFS spectra at the Cu K-edge for initial (t = 0 s), intermediate (30-40 s), and final (140-150 s) states and Fig. 21(b) indicates the time dependence of the absorption intensity at 8983 eV (the vertical broken line in Fig. 21(a)). As can be clearly seen in Fig. 21(b), there are two chemical reaction processes taking place. One is a rapid reaction, the creation process of an intermediate state which occurs within several seconds. The other is a slow reaction, where the intermediate state repopulates the initial state over a period of 100-200 s. Figures 21(c) and (d) show DXAFS spectra recorded during these two reaction processes. From these XAFS spectra, it is clear that Cu(II) is reduced to Cu(I) in the intermediate state. Full details of the scientific results obtained by this experiment will be presented elsewhere. It should be emphasized here that each DXAFS spectrum was measured with an exposure time of only 6 ms, but that the statistical error is sufficiently small. This means that detailed information can be obtained for a non-reversible chemical reaction within several tens of milliseconds. For a reversible chemical reaction, it is in principal possible to observe the reaction on a time scale of 100 ps, the bunch length at the PF-AR. Such studies are the main scientific subject for this beamline. In order to realize such time-resolution, two kinds of detectors are under development.

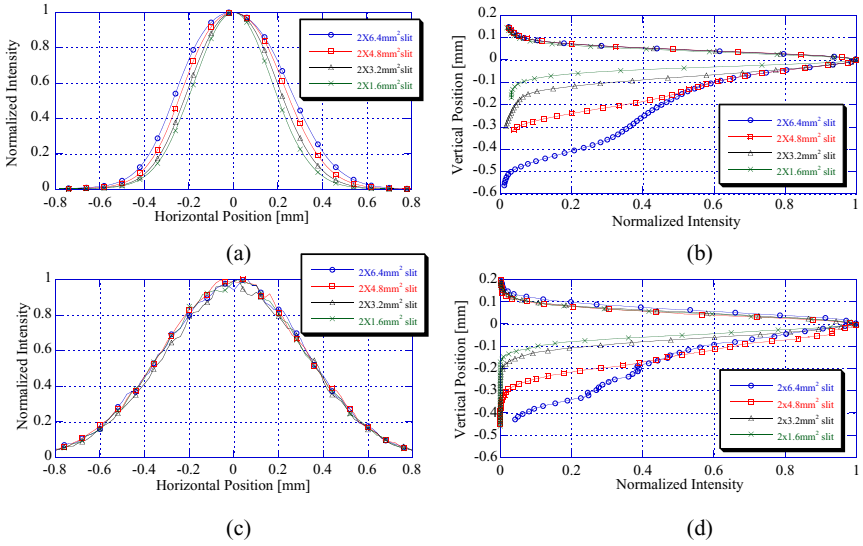

Figure 19
Comparison between the experimentally obtained focused beam profiles (a and b) and those obtained by a ray-tracing calculation (c and d). The opening sizes of the aperture at 16 m from the undulator source are indicated.

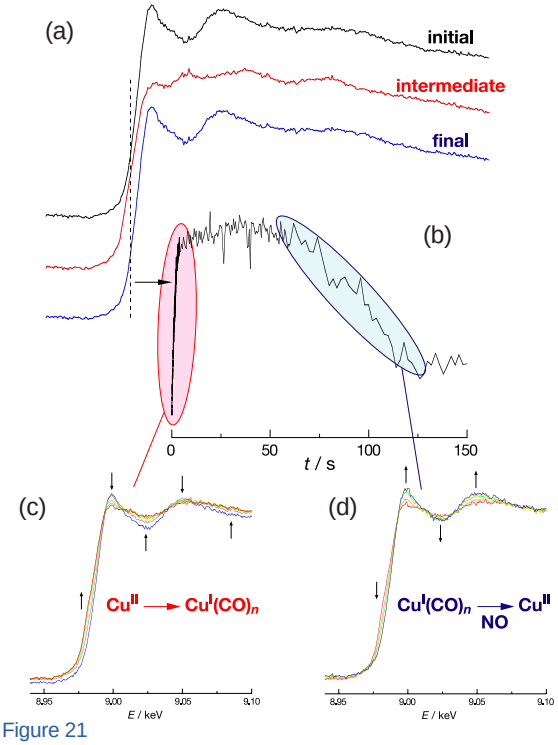

Figure 21
Time-resolved energy-dispersive XAFS spectra recorded during a reaction proceses of the Cu/ZSM-5 catalyst.

One is an X-ray CCD system working under kinetics mode, where one line is used as a linear detector and others are used for charge memory. The other detector system is a silicon microstrip detector called XSTRIP. Both will be introduced in 2006.

Besides time-resolved XAFS, the commissioning of a new experimental system for time-resolved diffraction experiments was carried out. The aim of this system is to reveal the structural changes of many interesting materials with the photo-induced phase transition technique. The first pump and probe measurements were carried out in the beginning of 2004 using fs and ns lasers (Fig. 22). Since a dedicated beamline for time-resolved X-ray diffraction was constructed in 2005, this activity has now been moved to AR-NW14A.

Figure 22
The green box is an experimental hutch and the black box is a laser hutch. The hutches are connected by a black pipe for transport of the laser beam.

4-2-6 Hard X-ray XAFS/AXS AR-NW10A

Construction of a hard X-ray XAFS and anomalous X-ray scattering (AXS) beam line AR-NW10A was approved by the Photon Factory Program Advisory Committee in 2005. Following this approval, the design and construction work was carried out. The first beam was introduced on Januray 17 2006, and the commissioning and evaluation of the beam line is currently in progress. The beamline will be open for public users from spring 2006.

BL-10B has been used by many users as a XAFS beam line in the rather hard X-ray region of 6 to 33 keV. It has been a workhorse in the Photon Factory and more than 1,020 publications have been registered in the Photon Factory publication database at the time of writing (January 2006). However, it was constructed in 1982 as the first XAFS beam line at the Photon Factory and is becoming less competitive. For example, the flux above 20 keV is not sufficient since the critical energy of the bending radiation from the 2.5-GeV PF ring is only 4 keV. Furthermore, the optical design is rather old and has no focusing system, the monochromator is getting less reliable, and the experimental hutch is very narrow. Thus the XAFS user community has been looking for the opportunity to construct a new XAFS beam line for the high energy region. Fortunately, Prof. Kiyotaka Asakura of Hokkaido University obtained funding from the JSPS for the study of the dynamics of catalytic reactions. It is very important to fabricate quick XAFS capabilities for this work and he kindly offered to use part of the funding for construction of a new beamline.

AR-NW10A uses radiation from a bending magnet in the 6.5 GeV PF-AR and covers the energy range between 8 and 42 keV, complimentary to the other XAFS stations as shown in Fig. 23. Since the critical energy is 26.3 keV, similar to SPring-8's 28.9 keV, a flux at 30 keV 75 times higher than that at BL-10B is expected. The optical design is rather simple, consisting of a Si(311) double-crystal monochromator and a Pt-coated bent cylindrical mirror. Since Rh-coated mirrors are usually used, XAFS experiments at the Rh edge are becoming difficult in Japan. Pt was chosen in order to cover a higher energy region and to provide the possibility of carrying out Rh XAFS experiments. Although

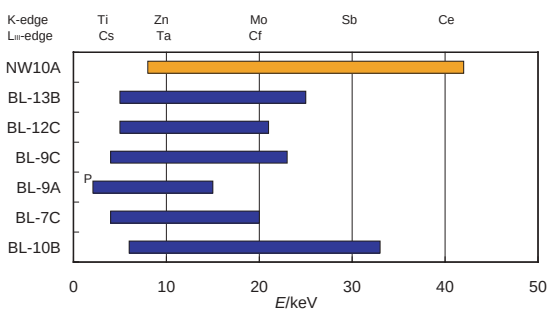

Figure 23
Avaiable energy range at XAFS expeerimental stations of PF and PF-AR.

there are platinum absorption edges between 11.5 and 13.9 keV, they will not become a serious problem for XAFS experiments since the irradiation angle is only 1.9 mrad. As mentioned above, the double-crystal monochromator has a quick XAFS capability and spectra can be obtained in less than a minute in the rather high energy region.

The experimental hutch is designed to meet the requirements for XAFS experiments to follow in-situ reactions. The experimental table on which both XAFS and AXS equipments are placed is fairly large, 1.2 m wide and 2 m long, and the two setups can be swapped fairly easily.

4-2-7 AR-NW12A (Protein crystallography)

outline

AR-NW12A is a new protein crystallography beamline at the PF-AR designed for high-throughput MAD experiments. Construction was completed in FY2002 and the first beam was observed on September 30 2002. After commissioning of the beamline components, NW12A was opened for public use in May 2003.

Light source and optics

For high-throughput MAD experiments, both high beam intensity and good energy tunability are required. To meet these requirements, the beamline was designed with the following specifications.

1) An in-vacuum tapered undulator is used as the source providing a high-flux X-ray beam optimized at around 12.7 keV using the 3rd harmonic.
2) A bent-flat collimating mirror and a liquid nitrogen circulation system for cooling the monochromator crystals are used to achieve good energy resolution.
3) The monochromator consists of double flat Si (111) crystals and covers a wide energy range from 7 to 17 keV with a fixed beam exit mechanism.
4) A bent-cylindrical mirror focuses the beam onto the sample position in both horizontal and vertical directions. The location of the mirror is chosen to realize 2:1 focusing, and hence reduce the beam divergence.

Figure 24 shows the plan view of the beam line. The front-end consists of a fixed mask, a beam-position monitor, an absorber, a beam shutter, graphite heat ab-

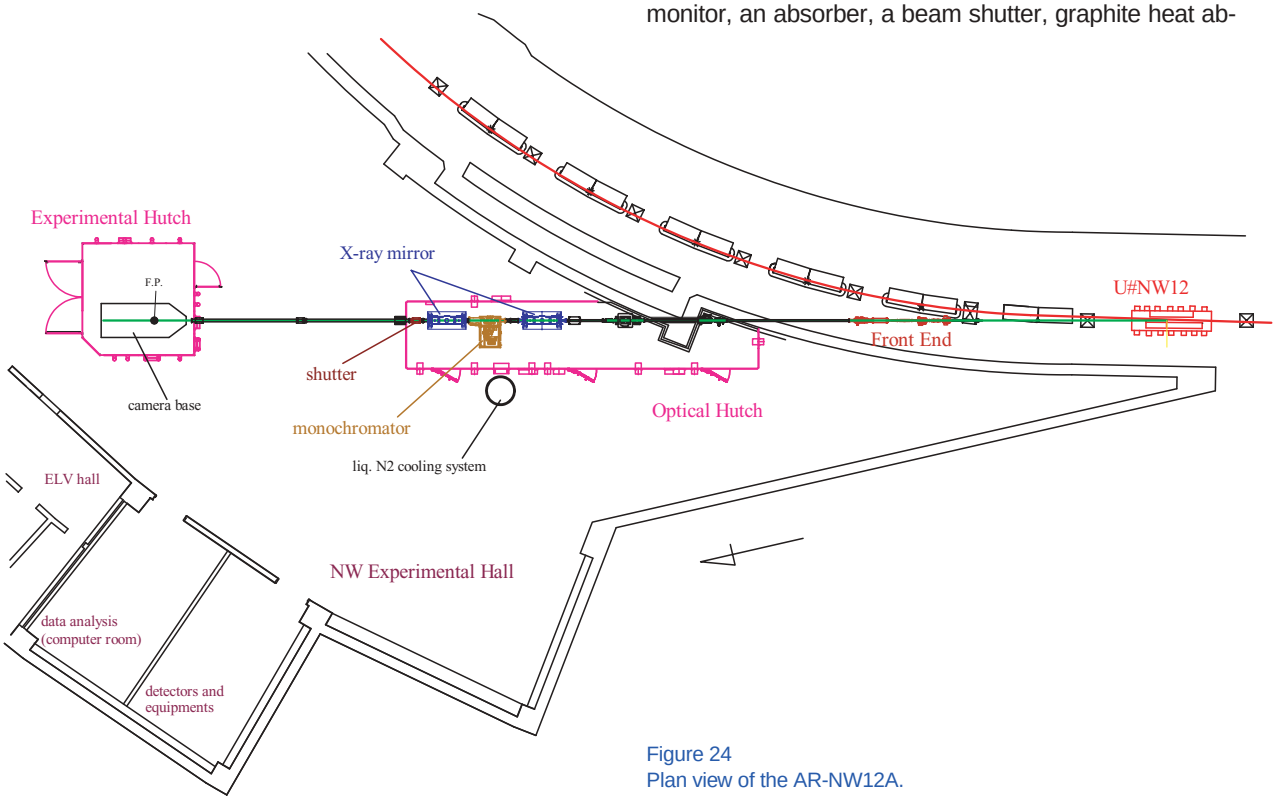

Figure 24
Plan view of the AR-NW12A.

Table 4 Specification of the optical components.

Insertion device	Type: tapered undulator Length of period: 40 mm Number of periods: 95 Magnetic field: max 0.6 Tesla Energy range: 7-17 keV with the 3rd harmonics
Collimating mirror (23.5 m from the source)	Type: flat-bent Material: Rh-coated Si single crystal Size (mm): 1000(L) × 100(W) × 70(T) Glancing angle: 3.5 mrad Radius of curvature: 13428.6 m Slope error(μrad): max. 1.56 (L), 5.71(W) Roughness: max. 1.34 A
Double crystal monochromator (25.4 m)	Material: Si(111) Fixed exit: numerical link Cooling system: liquid nitrogen circulation Energy range: 7 – 17 keV
Focusing mirror (27.0 m)	Type: bent-cylindrical Material: Rh-coated Si single crystal Size(mm): 1000(L) × 100(W) × 70(T) Radius of curvature: 54.76 mm, 6285.7 m Glancing angle: 3.5 mrad Slope error(μrad): max. 3.37(L), 5.93(W) Roughness: max. 1.61 A

sorbers, XY-slits for white X-rays and Be windows. The location and specification of the main optical components are summarized in Table 4. The specifications of the undulator and the monochromator are almost same as those installed in AR-NW2A.

Characteristics of the beam at the sample position are summarized in Table 5. The energy resolution of the beam was estimated from the full-width at half-maximum of the rocking curve with Si(111). The beam size was measured by silt scanning with a 200 μm window. The beam intensity was estimated using a PIN photodiode to be higher than 10^{11} photons/sec at the sample position, with 200 × 200 μm slit and 0.5 mrad beam divergence. The expected values calculated using ray-tracing techniques are also shown in Table 5 and show reasonable agreement to the measured parameters.

Experimental station

A CCD-type X-ray detector ADSC Q210 was installed in the experimental hutch. The active area of the detector is 210 mm^2 and the positional resolution is 51 microns. Combined with the gigabit Ethernet network, the dead time including read-out is around 2.0 sec per frame. This means the time required for collecting one data set (1degree oscillation and 180 frames) is around 20 min with a 5 sec exposure time, typical for undulator beamlines. For four-wavelength MAD, it takes 1 or 2 hours (including XAFS measurements) to complete the data collection, around 10 times faster than at existing bending magnet beamlines such as BL-6A or old BL-18B.

The experimental table has an attenuator, four-blade slits, a high-speed shutter and one-axis high-precision goniometer in front of the detector. The shutter can control exposure times of 1 msec, and the fluctuation of the sample axis is only 2.3 microns, matching well to measurements with crystals of micron-size. The shutter timing is synchronized with the rotation of the goniometer axis to achieve accurate oscillation measurement. All the equipment including beam stopper, fluorescent detector, and telescope is motorized to enable automatic remote experiments.

Table 5 Characteristics of the beam.

	Measured	Simulated
ΔE/E at 12.7 keV	2.5×10^{-4}	1.48×10^{-4}
Beam size at sample position (μm)	1.4(H) 0.18(V)	1.469(H) 0.226(V)
Photons/sec at sample position (through 0.2 mm square slit)	2.0×10^{11}	5.5×10^{11}

Scientific activities

—Crystal Structure of the Ankyrin Repeat Domain of Human Ribonuclease L —

Interferons (IFNs) are proteins with antiviral, antitumor, and immunomodulatory activities. In the interferon-induced 2-5A system [6], treatment of cells with IFN activates genes encoding several 2',5'-linked oligoadenylate synthetases (OASs) and a single gene encoding ribonuclease L (RNase L). The OASs are activated by binding to dsRNA and generate 5'-phosphorylated, 2',5'-phosphodiester-linked oligoadenylate (2-5A) from ATP. RNase L is activated by binding to 2-5A, changing from an inactive monomer to a catalytically active homodimer. The activated RNase L cleaves viral RNA, and the RNA degradation inhibits protein synthesis and thus inhibits viral replication. The human form of RNase L is a 741-amino acid protein [7]. RNase L consists of three domains, namely the N-terminal ankyrin repeat domain, the protein kinase homology domain, and the C-terminal ribonuclease domain. The N-terminal ankyrin repeat domain is responsible for 2-5A binding, and the C-terminal domain is responsible for catalytic activity. To elucidate the structural basis for 2-5A-dependent dimerization and activation of RNase L, we initiated the structural studies of human RNase L. Recently, we have determined the crystal structure of the N-terminal ankyrin repeat domain (ANK) of human RNase L complexed with 2-5A [8,9].

Crystals of ANK were obtained in the presence of a 2-5A trimer with 5'-monophosphate (Fig. 5). The crystals belong to an orthorhombic space group P212121 with cell dimensions of a = 63.20 Å, b = 72.83 Å, and c = 82.63 Å. Data collection was preformed at 100 K using synchrotron radiation from AR-NW12. The crystal structure of ANK/2-5A complex was determined by the molecular replacement method, and we refined the resulting model to an R-factor of 0.202 (free R-factor of 0.230) at 1.8 Å resolution. The final model consisted of residues 21-305, 220 water molecules, and one 2-5A molecule [8].

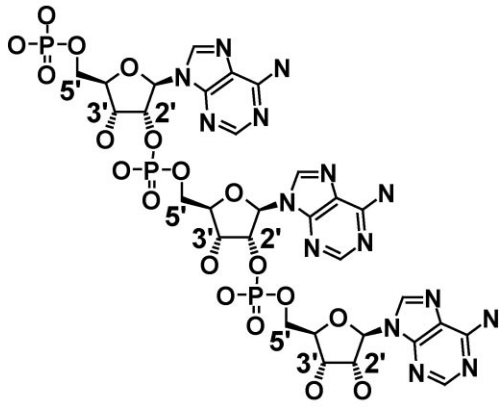

Figure 25
Structure of 5'-monophosphate-type 2-5A used for the present crystal structure analysis.

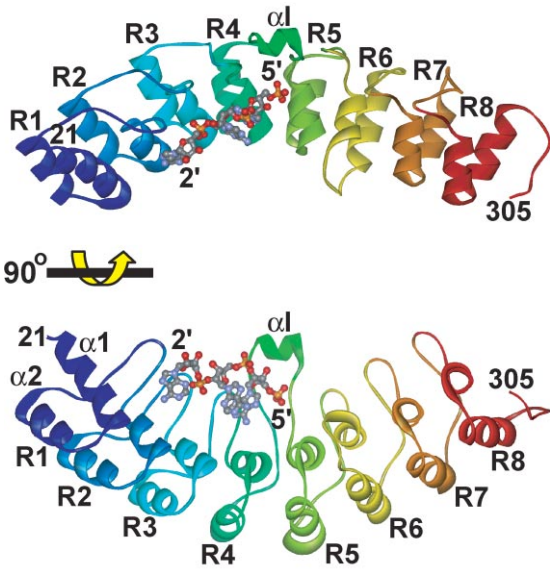

Figure 26
Ribbon representations of the ANK/2-5A complex. The bound 2-5A molecule is shown as a ball-and-stick model.

ANK folds into eight ankyrin repeat elements and forms an extended curved structure with a groove running across the long concave surface (Fig. 26). The 2-5A molecule is accommodated in the concavity and directly interacts with ankyrin repeats 2 to 4 (Fig. 27). Interestingly, the 2-5A binding residues in the repeat 4 (R4) and repeat 2 (R2) of ANK are located at the structurally equivalent position of the ankyrin repeat and these residues play a functionally equivalent role. The side chains of Arg155 in R4 and Lys89 in R2 form salt bridges with Phos1 and Phos3, respectively. The side chains of Phe126 in R4 and Trp60 in R2 stack with Ade1 and Ade3, respectively. The side chains of Glu131 in R4 and Asn65 in R2 form hydrogen bonds with Ade1 and Ade3, respectively. Furthermore, a quadruplex (Arg155-Phe126-Ade1-Ade2) and a triplex (Lys89-Trp60-Ade3) of stacking interactions are observed at R4 and R2, respectively.

Because the catalytically active form of RNase L is a potent antiviral and anticellular protein, stable derivatives of 2-5A able to penetrate cell membranes may eventually provide novel therapeutic agents for viral

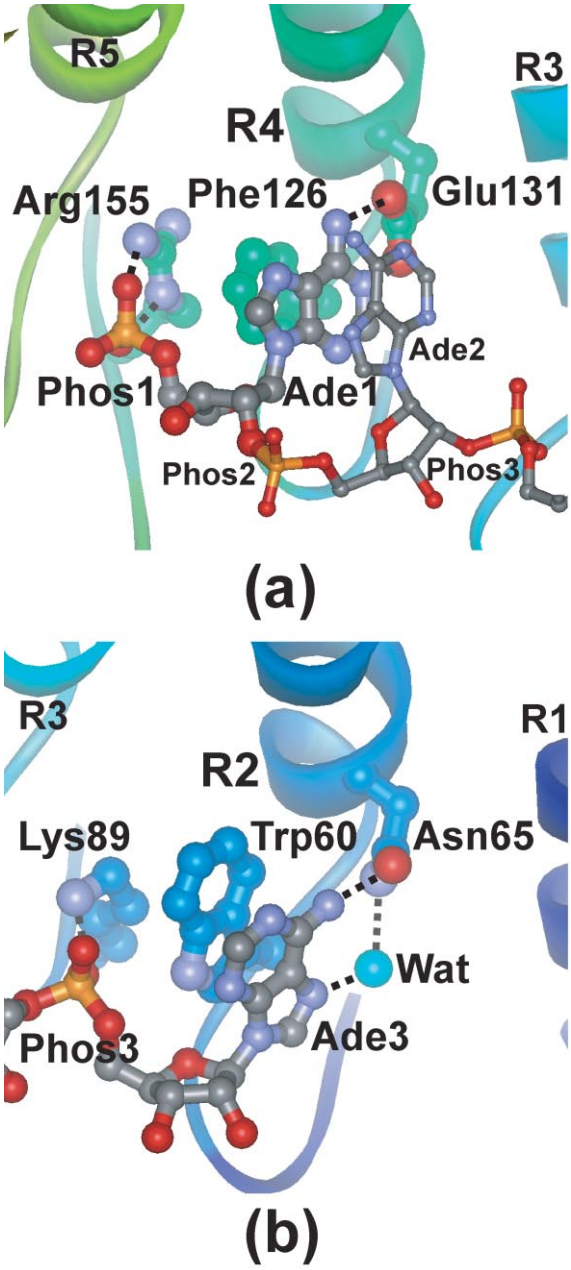

Figure 27
Recognition of the first and third AMP moiety of 2-5A by (a) repeat 4 and (b) repeat 2, respectively, of ANK.

infection and tumor development. Knowledge of the structural basis for 2-5A recognition by ANK is essential for designing stable 2-5As with a high likelihood of activating RNase L.

References

[6] M. R. Player and P. F. Torrence, *Pharmacol. Ther*., **78** (1998) 55.

[7] A. Zhou, B. A. Hassel and R. H. Silverman, *Cell,* **72** (1993) 753.

[8] N. Tanaka, M. Nakanishi, Y. Kusakabe, Y. Goto, Y. Kitade and K. T. Nakamura, *EMBO J*., **23** (2004) 3929.

[9] N. Tanaka, M. Nakanishi, Y. Kusakabe, Y. Goto, Y. Kitade and K. T. Nakamura, *Protein Peptide Lett.,* **12** (2005) 387.

4-2-8 AR-NW14A, A Beamline for Time-resolved X-ray Studies

AR-NW14A is a new insertion device beamline at the PF-AR aiming for time-resolved X-ray diffraction/scattering and XAFS. The primary scientific goal of this beamline is to observe the ultrafast dynamics of condensed matter such as organic and inorganic crystals, biological systems and liquids triggered by optical pulses. With the use of the high photon flux available from in-vacuum undulators, it should become possible to take snapshots of electron density distributions with 50-ps resolution.

The new beamline has two undulators with period lengths of 36 mm (U36) and 20 mm (U20) (Fig. 28). The U36 covers an energy range of 5-25 keV with its 1st, 3rd, and 5th harmonics, and is used as a tunable and intense monochromatic X-ray source by using a double-crystal monochromator and a focusing mirror. The typical photon flux of the monochromatic beam is estimated as ~10^{12} photons/sec. The U20 has a 1st harmonic in the energy range of 13-20 keV with an energy bandwidth of $\Delta E/E$ ~10^{-1}-10^{-2}, allowing its use as a 'narrow-bandwidth white beam' or 'wide-bandwidth monochromatic beam' with a photon flux of ~10^{15} photons/sec. The X-ray pulses are delivered at a frequency of 794 kHz with a pulse duration of ~50 ps (rms). The focused beam size of monochromatized X-rays from the U36 at the sample position is estimated to be 0.2 mm (V) × 0.6 mm (H).

A plan view of the beamline is shown in Fig. 29. The front end consists of a fixed mask, a beam-position monitor, an absorber, a beam shutter, graphite heat absorbers, XY-slits for white X-rays and Be windows. The main optical components are a double-crystal monochromator and X-ray mirror system, which are located 30.5 m and 39-42 m from the center of the insertion device U20, respectively. The double-crystal monochromator consists of flat Si(111) crystals which are cooled with liquid nitrogen in order to reduce deformation caused by heat loads. The cooling system can handle an incoming heat load of up to 450 W. The X-ray mirror

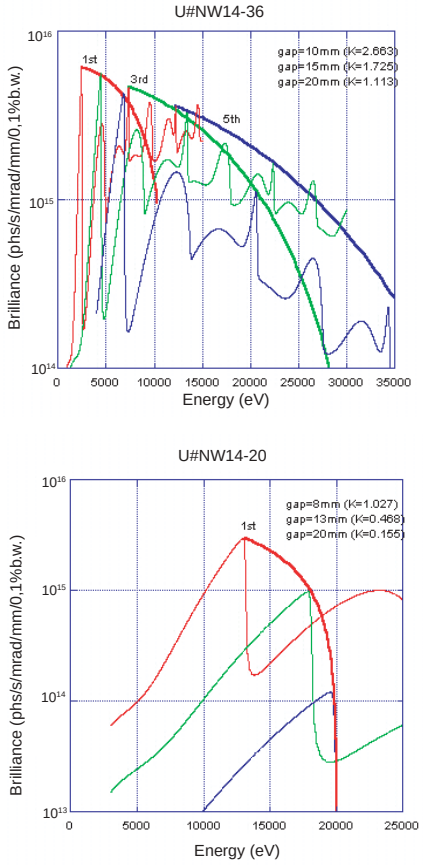

Figure 28
Spectra of U36 and U20 at NW14 (calculated by SPECTRA7.2).

system has 3 mirror assemblies: a bent cylindrical mirror for focusing of X-rays, and a double-mirror system (cut-off mirrors) to reduce contamination from the higher harmonics.

Construction of the experimental hutch and laser booth were completed by the end of July 2005. After the hutch construction, beamline components, diffractometers and a femtosecond laser system were installed in August 2005. Commissioning of the beamline components is now underway, and the beamline will be fully operational from January 2006.

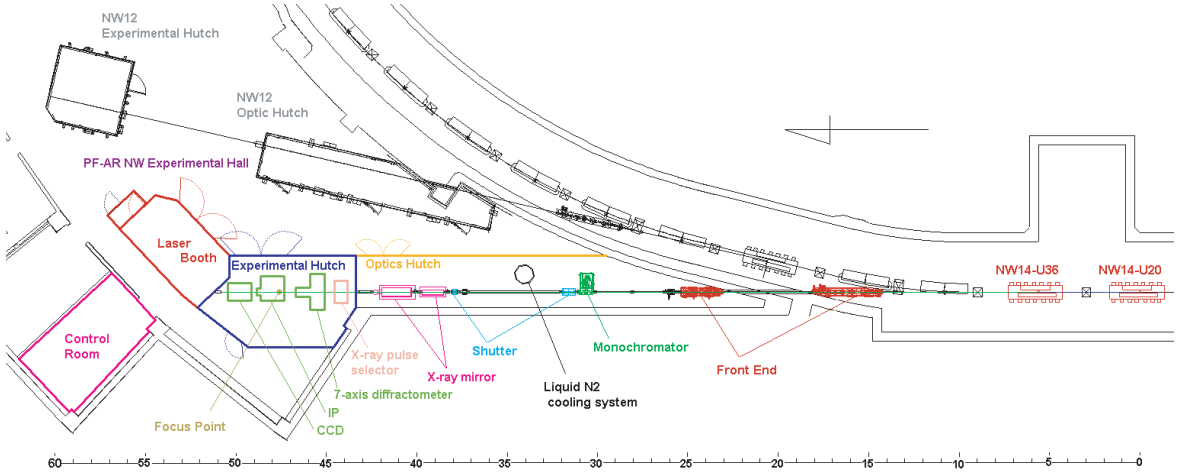

Figure 29
Plan view of AR-NW14A.

4-2-9 A High-Resolution ARPES Spectrometer Combined with a Combinatorial Laser MBE Thin Film Growth System

A high-resolution angle-resolved photoemission (ARPES) spectrometer combined with a combinatorial laser molecular-beam epitaxy (laser MBE) thin film growth system was constructed to investigate the electronic structure of transition metal oxide epitaxial thin films. The system is installed at either the high-resolution vacuum-ultraviolet beamline BL-1C or the soft-X-ray undulator beamline BL-2C. In this system (Fig. 30), laser MBE-grown thin film samples can be transferred into the photoemission chamber without breaking ultrahigh vacuum. Laser MBE is suitable for growing thin films of many different transition metal oxides with the well-ordered surfaces that are essential for ARPES measurements. The capability of the system was demonstrated with a study of the band structure of $La_{0.6}Sr_{0.4}MnO_3$ (LSMO) thin films.

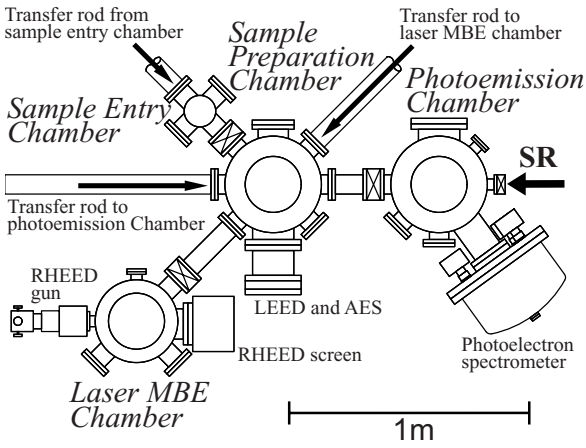

Figure 30.
A schematic diagram of an *in situ* ARPES-laser MBE system.

The growth and ARPES measurement of $La_{0.6}Sr_{0.4}MnO_3$ thin films using the in situ ARPES-laser MBE system were performed at BL-1C. LSMO thin films with a thickness of about 40 nm were deposited on TiO_2-terminated $SrTiO_3$(001) substrates. Epitaxial growth of LSMO thin films was confirmed by the observation of clear RHEED oscillations. The ARPES spectra were recorded at 150 K using a GAMMADATA SCIENTA SES-100 electron-energy analyzer. The surface morphology of the films was analyzed by ex situ atomic force microscopy in air and an atomically flat step-and-terrace structure was observed. Fig. 31(b) shows ARPES spectra of an LSMO thin film recorded at various photon energies between 30 and 70 eV at normal emission. We find that the ARPES spectra exhibit considerable and systematic changes as a function of photon energy; highly dispersive features with a bandwidth of about 2 eV exist in the energy range of 2-5 eV. Figure 31(c) shows the experimental band structure of LSMO thin films along the G–X direction in the Brillouin zone of the cubic perovskite structure derived from the present normal emission ARPES measurement. The dark areas of the plot correspond to the energy bands. As expected from the ARPES spectra, several dispersive bands are clearly observed, demonstrating that we have succeeded in the ARPES measurement of LSMO thin films.

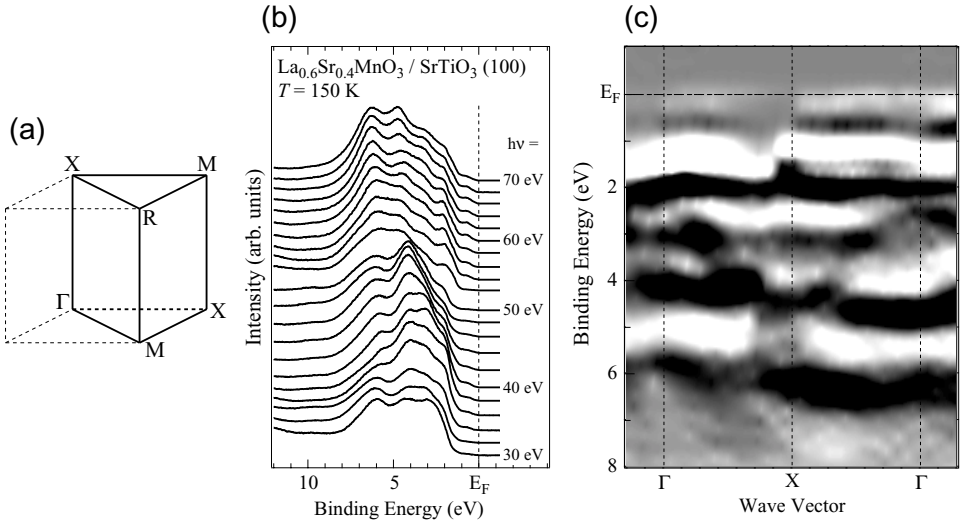

Figure 31
(a) Brilouin zone of cubic perovskite structure. (b) ARPES of a LSMO epitaxial thin film grown by laser MBE. (c) Experimental band structure of the LSMO thin film. Dark areas correspond the energy bands.

4-2-10 Individual Cell Irradiation System for Radiobiology using Microbeam

Risk evaluations of low dose or low dose rate irradiation are of great concern for human societies utilizing modern technologies. The energy of incident radiation is converted to kinetic energy of secondary charged particles and subsequently deposited into molecules in the cellular system. The energy deposited in a cell, the dose, is proportional to the number of particles traversing the cell. In the low dose region, the average number of tracks per cell becomes small and hence the number shows the Poisson distribution. From the characteristics of the Poisson distribution, the fraction of cells that have not accepted any track at all is 37% when the average track number is unity. In even lower dose regions, the number of un-hit cells becomes much larger than the number of hit cells. Observation of total cell population without knowing the distribution of hit and un-hit cells gives very little knowledge of the mechanisms of cellular response to low dose environmental radiation. To study the radiation response of the cell it is necessary to know whether individual cells have been irradiated or not. From this motivation, microbeam irradiation systems using particle (He^{2+} or proton) beams have been developed in the UK and USA. According to reports from these studies, it has been found that un-hit cells situated nearby to irradiated cell exhibit certain responses to the radiation (bystander effects). This type of response can only be observed when individual cells are identified and irradiated with the desired amount of dose using microbeams of about a few microns in diameter.

Considering that we are exposed to γ- or X-ray photons more often than to high-energy heavy particles in our living environment, we have developed a microbeam irradiation system using monochromatic synchrotron X-rays in order to study radiation responses to low dose X-rays. In contrast to He^{2+} particle irradiation where the minimum dose to the cell is order of 0.1 Gy, 5.35 keV photon beams can deliver does as small as 1 mGy, indicating that the photon microbeam is preferable for research into low-dose radiation effects.

Designed system

The proposed system is composed of three parts, and the whole system is schematically shown in Fig. 32. First is a Kirkpatrick-Baez (K-B) mirror system to focus the X-ray beam to a size of 1 mm diameter. The beam is reflected at right angles upwards by a silicon crystal (311), which determines the energy of the X-rays to be 5.35 keV. The range of photoelectrons generated with X-rays of this energy is about 0.8 μm. Secondly, a fluorescence microscope is equipped with a precise automatic stage on which the sample dish is fixed and irradiated with the focused X-ray beam from below. The third component of the system is a fluorescence image analyzer (computer) with a sensitive CCD camera which can recognize the target cells and their positions. This computer also controls the irradiation to the target cells by the X-ray beam one by one, automatically. The proposed throughput is 1000 cells per hour in order to keep the cells in good physiological condition during the irradiation procedure.

The system has been installed at BL-27B. Experimental stations at BL-27 are situated in the biological sample preparation area, where incubators and other equipments to grow and keep mammalian cells are available.

Performance of the photon microbeam irradiation system

—X-ray energy and beam size—

We have confirmed that our K-B mirror system acts as designed. A knife-edge scan at the focus point showed an FWHM at the focus point of 2 microns when a 20-μm pinhole was used as a pseudo light source. Due to the complexity of setting up the mirror system however, we use a slit system to obtain the microbeam, and the beam size available is 5 μm2 or larger (adjust-

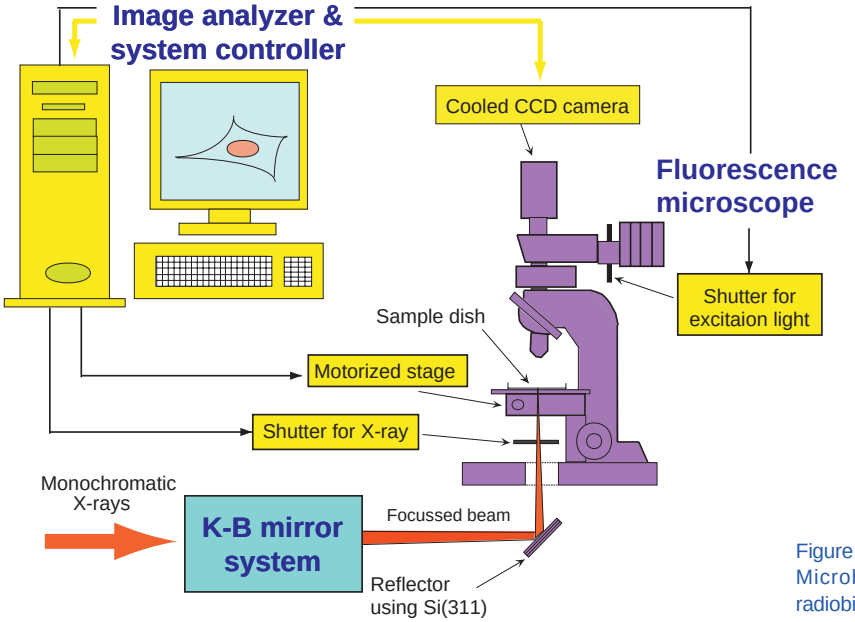

Figure 32
Microbeam irradiation system for radiobiology at Photon Factory.

able). The size is small enough to aim at intracellular organelles such as nuclei. The dose rate is about 6 Gy/min, independent of the beam size.

—Cell recognition and positioning—

Cells to be irradiated are stained with appropriate dilute fluorescent dyes and their fluorescence images captured with a CCD camera and analyzed with appropriate software to recognize cells or nuclei within cells. Positions are calculated and memorized for the positioning of the targets to be irradiated.

—Accuracy/reproducibility of the target positioning—

The motorized precision stage we adopted is equipped with linear encoders of 0.5-μm accuracy. However, the overall reproducibility of the system is determined also by the distortion of the components in the imaging system, such as the optical distortion in the image field of the microscope and the positional deviation of pixels in the CCD camera. In order to check the accuracy of the obtained coordinates of the target, we have tested the accuracy/reproducibility of the targeting using fluorescent micro-spheres (5 μm in diameter) immobilized on a dish. The average deviation was 1.5 μm a value considered small enough to aim at individual cell nuclei.

We also tested whether the sample cells could be found and identified when the sample dish was replaced in the system following various post-irradiation treatments. It was found that irradiated targets could easily be identified on the sample dish once detached after irradiation.

—System control software—

We have developed software written with Visual Basic, calling ImageProPlus as a subroutine. The software can control all the processes including image-capture, image analysis, stage movement and X-ray irradiation.

A photograph of the whole system is shown in Fig. 33.

Results typical of those obtained so far are shown in Fig. 34. We have succeeded in observing the γ-H2AX immuno-staining of irradiated cell nuclei, used to identify double strand breaks in DNA. We could easily identify the irradiated cells and could recognize the size of the beam used for irradiation of the targetted cell nuclei. A more sophisticated mode in which the designated area is scanned to search for the target and automatically irradiate with the desired X-ray dose has also been developed and is being used to obtain the dose-survival relationship.

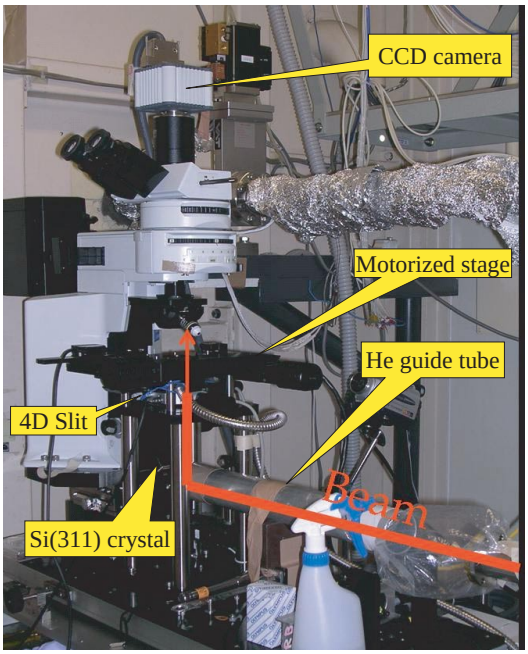

Figure 33
Photograph of the developed microbeam irradiation system setup at BL-27B.

(a)

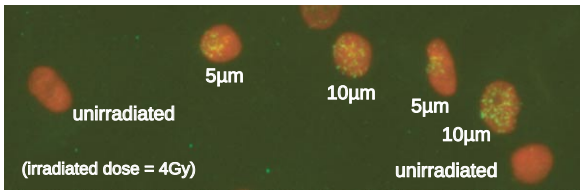

(b)

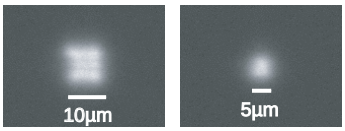

Figure 34
Panel (a), Fluorescent image of human fibroblast cells. All the cell nuclei were stained with propydium iodide(PI) and appear red in color. Phospholyrated histon H2AX (γ-H2AX), induced as the result of the production of DNA double strand breaks by X-rays, were observed in green by staining with the secondary antibody FITC of γ-H2AX.
Panel (b), Images of the X-ray microbeam of 10 μm square and of 5 mm square, visualized by scintilator set on the sample dish. Magnification scale was the same as with panel (a).
Panel (b), Images of the X-ray microbeam of 10 μm square and of 5 μm square, visualized by scintilater set on the sample dish. Magnification scale was the same with panel (a).

4-2-11 Slow Positron Facility (SPF)

Introduction

Positron spectroscopy based on intense positron sources such as electron-linac based sources offers a new methodology for not only positron research but also for solid state physics, atomic and molecular science, biological science and other related sciences. The facility was constructed during FY2001-FY2002. In FY2003 additional radiation shields were installed and a slow positron transport line was commissioned. Preliminary experiments were made by users under Joint Development Research at KEK, starting in October 2003. The facility has been available for public use since April 2004, and five research groups are currently performing new experiments.

Facility

Figure 35 shows a plan view of the Slow Positron Facility experimental hall at the underground level of the Linac building. The next-generation slow positron generator is installed upstream of the slow positron beamline. The energetic electrons from the linac produce bremsstrahlung photons in a water-cooled tantalum target of 2-mm thickness, resulting in the pair creation of electrons and positrons. The energetic positrons are slowed down in seven sheets of tungsten converter of 25 μm thickness which have been well annealed at 2273 K under UHV conditions. The assembly has a Wehnelt element with a photo-chemically manufactured grid to extract slow positrons.

The extracted slow positrons are guided by an axial magnetic field of 60 G. Two Penning-trap electrodes separated by 7.2 m are installed in the straight section for future conversion of the pulsed beam to a dc-like beam.

At the downstream end of the beamline, a Ps-TOF spectroscopy station is installed. The parameters of the Ps-TOF line are summarized in Table 6.

A schematic diagram of the Ps-TOF experiment is shown in Fig. 36. The sample bias is varied in the range of 0~9.5 kV using a retarding electrode (RET), and the distance between the sample and the detector is adjusted by moving the sample with a linear transfer. The pulse heights and detection time of annihilation g rays from annihilation events are recorded by a digital oscilloscope (LeCroy Wavepro 960). An example of the Ps-TOF spectrum of Al_2O_3/Al is presented in Fig. 37 where the ordinate represents pulse counts and the abscissa represents detection time relative to time zero, set by

Table 6 Parameters of the Ps-TOF line.

Parameter	
Intensity	2×10^5 [e^+/pulse]
Beam energy	0.1 - 30 [keV]
Pulse width	22 [ns] (FWHM) at 5.0 keV
Repetition rate	50 [Hz]
Beam diameter	10 [mm]
Sample temperature	Room temp.
Sample potential	0 - 9.5 [kV]
Vacuum pressure	10^{-7} [Pa]

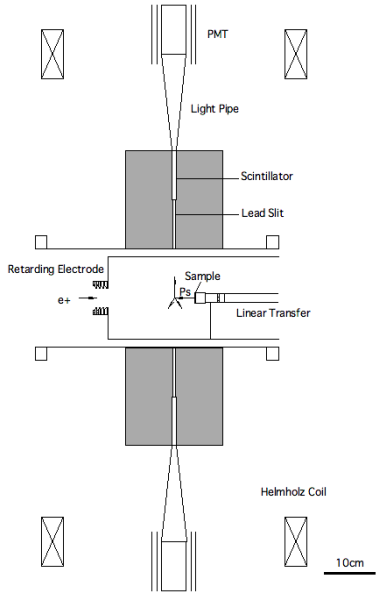

Figure 36
Ps-TOF experimental setup.

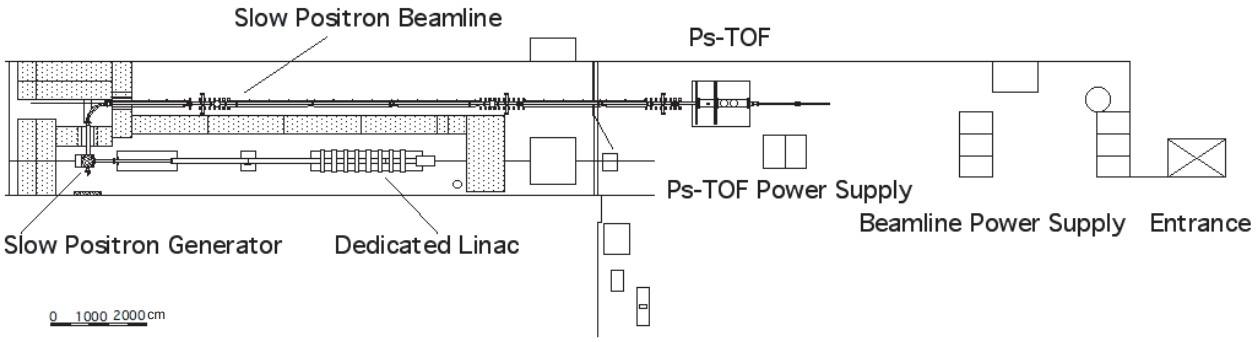

Figure 35
Schematic view of 50MeV linac, the slow positron generator assembly, the slow positron transport line and the experimental station for positronium time-of-flight (Ps-TOF) spectroscopy.

a trigger pulse from the linac. The detection of photons from 2g annihilation events in the specimen are detected at around 80 ns, while g rays of various energies due to the decay of traveling Ps are seen at later times.

Positronium emission from the surface is most efficiently detected by the implantation of a 0.4 keV positron beam (peak around 200 ns in Fig. 37). The center of the positronium emission peak appears at later times when the implantation energy of positron is increased, and the positronium yield decreases as the positron penetrates deeper through the surface. This phenomenon reveals the structure of the surface of the sample.

The dedicated Linac has been operated by the KEK Accelerator Research group and their contributions to the slow positron facility are highly appreciated. We are also very grateful to Profs. Hyodo and Nagashima for their contributions to the design and construction of the Ps-TOF spectrometer.

Users and Topics

We have five users groups in FY2004. These users and staff get together to promote research in the fields of Bose-Einstein condensation effects, semiconductor industry related materials and R & D of positron radiography and positron imaging.

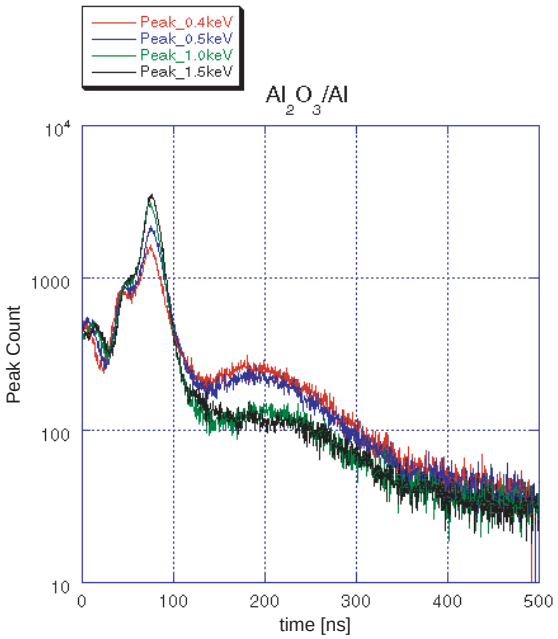

Figure 37
Obtained Ps-TOF spectrum of Al_2O_3/Al sample with different incident positron energies, ranging from 0.4 keV to 1.5 keV.